Available online at www.sciencedirect.com
SCIENCE DIRECT®
Journal of Sound and Vibration 284 (2005) 23–49
JOURNAL OF SOUND AND VIBRATION
www.elsevier.com/locate/jsvi

Modeling and analysis of a cracked composite cantilever beam vibrating in coupled bending and torsion

Kaihong Wang[a], Daniel J. Inman[a,*], Charles R. Farrar[b]

[a]*Department of Mechanical Engineering, Center for Intelligent Material Systems and Structures, Virginia Polytechnic Institute and State University, 310 Durham Hall, Blacksburg, VA 24061-0261, USA*
[b]*Los Alamos National Laboratory, Engineering Sciences and Applications Division, Los Alamos, NM 87545, USA*

Received 1 October 2003; accepted 4 June 2004
Available online 8 December 2004

Abstract

The coupled bending and torsional vibration of a fiber-reinforced composite cantilever with an edge surface crack is investigated. The model is based on linear fracture mechanics, the Castigliano theorem and classical lamination theory. The crack is modeled with a local flexibility matrix such that the cantilever beam is replaced with two intact beams with the crack as the additional boundary condition. The coupling of bending and torsion can result from either the material properties or the surface crack. For the unidirectional fiber-reinforced composite, analysis indicates that changes in natural frequencies and the corresponding mode shapes depend on not only the crack location and ratio, but also the material properties (fiber orientation, fiber volume fraction). The frequency spectrum along with changes in mode shapes may help detect a possible surface crack (location and magnitude) of the composite structure, such as a high aspect ratio aircraft wing. The coupling of bending and torsion due to a surface crack may serve as a damage prognosis tool of a composite wing that is initially designed with bending and torsion decoupled by noting the effect of the crack on the flutter speed of the aircraft.

*Corresponding author. Tel.: +1-540-231-2902; fax: +1-540-231-2903.
E-mail address: dinman@vt.edu (D.J. Inman).

0022-460X/$ - see front matter © 2004 Elsevier Ltd. All rights reserved.
doi:10.1016/j.jsv.2004.06.027

1. Introduction

Fiber-reinforced composite materials have been extensively used in high-performance structures where high strength-to-weight ratios are usually demanded, such as applications in aerospace structures and high-speed turbine machinery. As one of the failure modes for the high-strength material, crack initiation and propagation in the fiber-reinforced composite have long been an important topic in composite and fracture mechanics communities [1]. Cracks in a structure reduce the local stiffness such that the change of vibration characteristics (natural frequencies, mode shapes, damping, etc.) may be used to detect the crack location and even its size. A large amount of research was reported in recent decades in the area of structural health monitoring, and literature surveys can be found for cracks in rotor dynamics [2], and in beam/plate/rotor structures [3]. To prevent possible catastrophic failure when initial cracks grow to some critical level, early detection and prognosis of the damage is considered a valuable task for on-line structural health monitoring.

Compared to vast literature on crack effects to isotropic and homogeneous structures, much less investigation on dynamics of cracked composite structures was reported, possibly due to the increased complexity of anisotropy and heterogeneity nature of the material. In late 1970s, Cawley and Adams [4] detected damage in composite structures based on the frequency measurement. The concept of local flexibility matrix for modeling cracks [5] was extended to investigate cracked composite structures by Nikpour and Dimarogonas [6]. The energy release rate for the unidirectional composite plate was derived with an additional coupled term of the crack opening mode and sliding mode. The coefficient of each mode as well as of the mixed interlocking deflection mode in the energy release equation is determined as a function of the fiber orientation and volume fraction. The anisotropy of the composite greatly affects the coefficients. Nikpour later applied the approach to investigate the buckling of edge-notched composite columns [7] and the detection of axisymmetric cracks in orthotropic cylindrical shells [8]. Effects of the surface crack on the Euler–Bernoulli composite beam was investigated by Krawczuk and Ostachowicz [9] considering the material properties (fiber orientation and volume fraction). Song et al. [10] studied the Timoshenko composite beam with multiple cracks based on the same approach of modeling cracks with the local flexibility. To avoid the nonlinear phenomenon of the closing crack, cracks in these papers mentioned above are all assumed open.

The motivation of this investigation stems from the fracture of composite wings in some unmanned aerial vehicles (UAVs) deployed in the last few years such as the Predator [11]. The relative large wing span and high aspect ratio are the usual design for the low-speed UAVs. Surface cracks and some delamination near the wing root are suspected as the main fracture failure for the aircraft under cyclic loading during normal flight or impact loading during maneuvering, taking off and landing. Vibration characteristics of the cracked composite wing could be important to the earlier detection and the prevention of catastrophe during flight. This paper investigates the crack effects to the vibration modes of a composite wing, considering also the effects of material properties. The local flexibility approach is implemented to model the crack, based on linear fracture mechanics and the Castigliano theorem. The wing is modeled with a high aspect ratio cantilever based on the classical lamination theory and the coupled bending–torsion model presented by Weisshaar [12]. Unidirectional fiber-reinforced composite is assumed. Analytical solutions with the first few natural frequencies and mode shapes are

presented. To the authors' knowledge, vibration of the cracked composite beam with the bending–torsion coupling has not been studied prior to the work presented in this paper.

2. The local flexibility matrix due to the crack

A crack on an elastic structure introduces a local flexibility that affects the dynamic response of the system and its stability. To establish the local flexibility matrix of the cracked member under generalized loading conditions, a prismatic bar with a transverse surface crack is considered as shown in Fig. 1. The crack has a uniform depth along the z-axis and the bar is loaded with an axial force P_1, shear forces P_2 and P_3, bending moments P_4 and P_5, and a torsional moment P_6.

Let the additional displacement be u_i along the direction of loading P_i and U the strain energy due to the crack. The Castigliano's theorem states that the additional displacement and strain energy are related by

$$u_i = \frac{\partial U}{\partial P_i},$$

where U has the form $U = \int_0^a J(\alpha)\,\mathrm{d}\alpha$, $J(\alpha) = \partial U/\partial\alpha$ is the strain energy release rate, and a is the crack depth. By the Paris equation, $u_i = \partial\left(\int_0^a J(\alpha)\,\mathrm{d}\alpha\right)/\partial P_i$, the local flexibility matrix $[c_{ij}]$ per unit width has the components

$$c_{ij} = \frac{\partial u_i}{\partial P_j} = \frac{\partial^2}{\partial P_i \partial P_j}\int_0^a J(\alpha)\,\mathrm{d}\alpha. \tag{1}$$

Fig. 2 illustrates a fiber-reinforced composite cantilever with an edge surface crack and unidirectional plies. For an isotropic composite material, Nikpour and Dimarogonas [6] derived the final equation for the strain energy release rate $J(\alpha)$ as

$$J = D_1\left(\sum_{n=1}^{6} K_{\mathrm{I}n}\right)^2 + D_2\left(\sum_{n=1}^{6} K_{\mathrm{II}n}\right)^2 + D_{12}\left(\sum_{n=1}^{6} K_{\mathrm{I}n}\right)\left(\sum_{n=1}^{6} K_{\mathrm{II}n}\right) + D_3\left(\sum_{n=1}^{6} K_{\mathrm{III}n}\right)^2, \tag{2}$$

where $K_{\mathrm{I}n}$, $K_{\mathrm{II}n}$, and $K_{\mathrm{III}n}$ are stress intensity factors (SIF) of mode I, II, and III, respectively, corresponding to the generalized loading P_n. Here, mode I is the crack opening mode in which the crack surfaces move apart in the direction perpendicular to the crack plane, while the other two

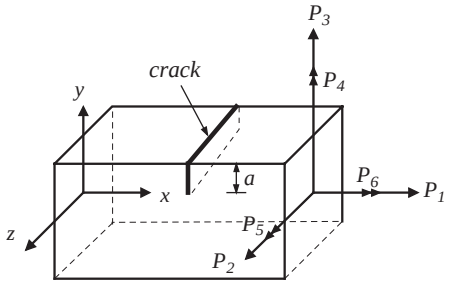

Fig. 1. A prismatic bar with a uniform surface crack under generalized loading conditions.

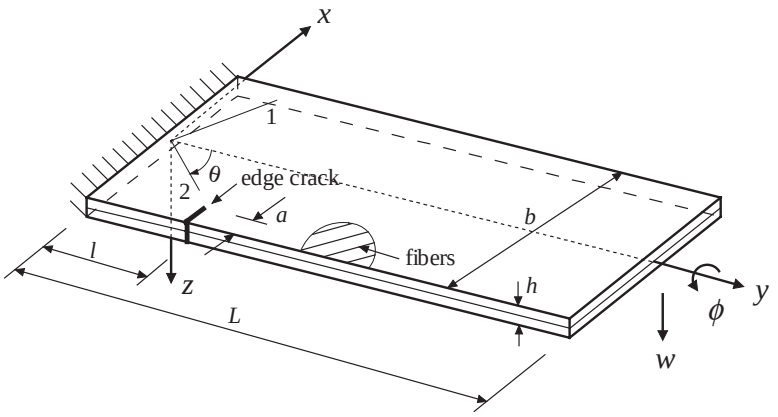

Fig. 2. Unidirectional fiber-reinforced composite cantilever with an open edge crack.

are associated with displacements in which the crack surfaces slide over one another in the direction perpendicular (mode II, or sliding mode), or parallel (mode III, or tearing mode) to the crack front. D_1, D_2, D_{12}, and D_3 are constants defined by

$$D_1 = -\frac{\bar{A}_{22}}{2}\,\mathrm{Im}\left(\frac{\mu_1+\mu_2}{\mu_1\mu_2}\right),\quad D_2 = \frac{\bar{A}_{11}}{2}\,\mathrm{Im}(\mu_1+\mu_2),$$

$$D_{12} = \bar{A}_{11}\,\mathrm{Im}(\mu_1\mu_2),\quad D_3 = \tfrac{1}{2}\sqrt{A_{44}A_{55}},$$

with μ_1 and μ_2 the roots of the characteristic Eq. (A.1) in Appendix A. Coefficients $\bar{A}_{11}$, $\bar{A}_{22}$, A_{44}, and A_{55} are also given in Appendix A. Note in Eq. (2) that the first two modes are mixed while the third mode is uncoupled from the first two modes if the material has a plane of symmetry parallel to the x–y plane, which is the case under investigation.

2.1. SIF

In general the SIFs $K_{jn}(j = I, II, III)$ cannot be taken in the same formats as the counterparts of an isotropic material in the same geometry and loading. Bao et al. [13] suggested that $K_{jn}(j = I, II, III)$ for a crack in the fiber-reinforced composite beam can be expressed as

$$K_{jn} = \sigma_n\sqrt{\pi a}F_{jn}(a/b,\ \tau^{1/4}L/b,\ \zeta), \tag{3}$$

where σ_n is the stress at the crack cross-section due to the nth independent force, a is the crack depth, F_{jn} denotes the correction function, L and b are the beam length and width, respectively, and τ and ζ are dimensionless parameters taking into account the in-plane orthotropy, which are defined by

$$\tau = \frac{E_{22}}{E_{11}},\quad \zeta = \frac{\sqrt{E_{22}E_{11}}}{2G_{12}} - \sqrt{\nu_{12}\nu_{21}},$$

where the elastic constants $E_{22}, E_{11}, G_{12}, \nu_{12}$, and ν_{21} are given in Appendix A.

Following the paper by Bao et al. [13], the term related to $\tau^{1/4}L/b$ is negligible for $\tau^{1/4}L/b \geqslant 2$. This condition is fulfilled for the fiber-reinforced composite cantilever in which the aspect ratio L/b is greater than 4. The SIF in Eq. (3) is then reduced to the form

$$K_{jn} = \sigma_n \sqrt{\pi a}\, Y_n(\zeta) F_{jn}(a/b), \tag{4}$$

where $Y_n(\zeta)$ takes into account the anisotropy of the material, and $F_{jn}(a/b)$ takes the same form as in an isotropic material and can be found from the handbook by Tada et al. [14] for different geometry and loading modes.

For the unidirectional fiber-reinforced composite beam, the SIFs are determined as

$$\begin{aligned}
&K_{\mathrm{I}1} = \sigma_1 \sqrt{\pi a}\, Y_{\mathrm{I}}(\zeta) F_1(a/b),\ \sigma_1 = \frac{P_1}{bh}, \quad K_{\mathrm{I}4} = \sigma_4 \sqrt{\pi a}\, Y_{\mathrm{I}}(\zeta) F_1(a/b),\ \sigma_4 = \frac{12P_4}{bh^3} z,\\
&K_{\mathrm{I}5} = \sigma_5 \sqrt{\pi a}\, Y_{\mathrm{I}}(\zeta) F_2(a/b),\ \sigma_5 = \frac{6P_5}{bh^2}, \quad K_{\mathrm{I}2} = K_{\mathrm{I}3} = K_{\mathrm{I}6} = 0,\\
&K_{\mathrm{II}3} = \sigma_3 \sqrt{\pi a}\, Y_{\mathrm{II}}(\zeta) F_{\mathrm{II}}(a/b),\ \sigma_3 = \frac{P_3}{bh}, \quad K_{\mathrm{II}1} = K_{\mathrm{II}2} = K_{\mathrm{II}4} = K_{\mathrm{II}5} = K_{\mathrm{II}6} = 0,\\
&K_{\mathrm{III}2} = \sigma_2 \sqrt{\pi a}\, Y_{\mathrm{III}}(\zeta) F_{\mathrm{III}}(a/b),\ \sigma_2 = \frac{P_2}{bh},\\
&K_{\mathrm{III}6} = \sigma_6 \sqrt{\pi a}\, Y_{\mathrm{III}}(\zeta) F_{\mathrm{III}}(a/b),\ \sigma_6 = \frac{24P_6\pi^3}{\pi^5 bh^2 - 192h^3} \cos\left(\frac{\pi}{h} z\right),\\
&K_{\mathrm{III}1} = K_{\mathrm{III}3} = K_{\mathrm{III}4} = K_{\mathrm{III}5} = 0,
\end{aligned} \tag{5}$$

where

$$F_1(a/b) = \sqrt{\frac{\tan\lambda}{\lambda}}\left[0.752 + 2.02(a/b) + 0.37(1 - \sin\lambda)^3\right] / \cos\lambda, \quad \lambda = \frac{\pi a}{2b},$$

$$F_2(a/b) = \sqrt{\frac{\tan\lambda}{\lambda}}\left[0.923 + 0.199(1 - \sin\lambda)^4\right] / \cos\lambda,$$

$$F_{\mathrm{II}}(a/b) = \left[1.122 - 0.561(a/b) + 0.085(a/b)^2 + 0.18(a/b)^3\right] \Big/ \sqrt{1 - a/b},$$

$$F_{\mathrm{III}}(a/b) = \sqrt{\frac{\tan\lambda}{\lambda}}$$

and

$$Y_{\mathrm{I}}(\zeta) = 1 + 0.1(\zeta - 1) - 0.016(\zeta - 1)^2 + 0.002(\zeta - 1)^3,$$

$$Y_{\mathrm{II}}(\zeta) = Y_{\mathrm{III}}(\zeta) = 1.$$

In Eq. (5), σ_6 is the stress along the short edge of the cross-section, determined using the classical theory of elasticity, as shown in Appendix B.

2.2. The local flexibility matrix

For the composite cantilever with an edge crack shown in Fig. 2, Eq. (1) becomes

$$c_{ij} = \frac{\partial^2}{\partial P_i \partial P_j} \int_{-h/2}^{h/2} \int_0^a J(\alpha)\, \mathrm{d}\alpha\, \mathrm{d}z. \tag{6}$$

Substitution of Eq. (2) in Eq. (6) yields

$$c_{ij} = \frac{\partial^2}{\partial P_i \partial P_j} \left\{ \int_{-h/2}^{h/2} \int_0^a [D_1(K_{\mathrm{I}1} + K_{\mathrm{I}4} + K_{\mathrm{I}5})^2 + D_2 K_{\mathrm{II}3}^2 + D_{12}(K_{\mathrm{I}1} + K_{\mathrm{I}4} + K_{\mathrm{I}5}) K_{\mathrm{II}3} + D_3(K_{\mathrm{III}2} + K_{\mathrm{III}6})^2]\, \mathrm{d}\alpha\, \mathrm{d}z \right\}. \tag{7}$$

For the composite cantilever under consideration, there are two independent variables—the transverse and torsional displacements, and one dependent variable—the rotational displacement of the cross-section. Correspondingly, the external forces the cantilever could take are the bending moment (P_4), the shear force (P_2) and the torsional moment (P_4) as shown in Fig. 1. Out of all components in the flexibility matrix only those related to $i, j = 2, 4, 6$ are needed. It can be shown that the matrix $[C]$ is symmetric and $c_{24} = c_{46} = 0$. Based on Eqs. (5) and (7) the components of interest in the local flexibility matrix $[C]$ can be determined as

$$\begin{aligned}
c_{22} &= \frac{2\pi D_3}{hb^2} \int_0^a \alpha [F_{\mathrm{III}}(\alpha/b)]^2\, \mathrm{d}\alpha = \frac{2\pi D_3}{h} \Lambda_{\mathrm{III}}, \\
c_{44} &= \frac{24\pi D_1}{h^3 b^2} \int_0^a \alpha [F_1(\alpha/b)]^2\, \mathrm{d}\alpha = \frac{24\pi D_1 Y_{\mathrm{I}}^2}{h^3} \Lambda_1, \\
c_{66} &= \frac{\pi D_3 (24\pi^3)^2 h}{(\pi^5 b h^2 - 192 h^3)^2} \int_0^a \alpha [F_{\mathrm{III}}(\alpha/b)]^2\, \mathrm{d}\alpha = \frac{576 D_3 \pi^7 h b^2}{(\pi^5 b h^2 - 192 h^3)^2} \Lambda_{\mathrm{III}}, \\
c_{26} = c_{62} &= \frac{96\pi^3 D_3}{b(\pi^5 b h^2 - 192 h^3)} \int_0^a \alpha [F_{\mathrm{III}}(\alpha/b)]^2\, \mathrm{d}\alpha = \frac{96\pi^3 D_3 b}{\pi^5 b h^2 - 192 h^3} \Lambda_{\mathrm{III}},
\end{aligned} \tag{8}$$

where the dimensionless coefficients are $\Lambda_{\mathrm{III}} = \int_0^{\bar{a}} \bar{\alpha} F_{\mathrm{III}}^2(\bar{\alpha})\, \mathrm{d}\bar{\alpha}$, $\Lambda_1 = \int_0^{\bar{a}} \bar{\alpha} F_1^2(\bar{\alpha})\, \mathrm{d}\bar{\alpha}$ and $\bar{a} = a/b$.

The final flexibility matrix [5,6] at the crack location for the coupled bending and torsional vibration is then

$$[C] = \begin{bmatrix} c_{22} & 0 & c_{26} \\ 0 & c_{44} & 0 \\ c_{26} & 0 & c_{66} \end{bmatrix}, \tag{9}$$

with components given in Eq. (8).

3. The composite beam model considering coupled bending and torsion

In the preliminary design, it is quite common that an aircraft wing is modeled as a slender beam or box to study the bending–torsion characteristics. Weisshaar [12] presented an idealized beam model for composite wings describing the coupled bending–torsion with three beam cross-sectional stiffness parameters along a spanwise mid-surface reference axis: the bending stiffness parameter EI; the torsional stiffness parameter GJ and the bending–torsion coupling parameter K. Note that EI and GJ are not the bending and torsion stiffness of the beam since the reference axis is not the elastic axis in general. At any cross-section of the beam as shown in Fig. 3 the relation between the internal bending moment M, the torsional moment T, and the beam curvature $\partial^2 w/\partial y^2$ and twisting rate $\partial\phi/\partial y$ is expressed as

$$\begin{Bmatrix} M \\ T \end{Bmatrix} = \begin{bmatrix} EI & -K \\ -K & GJ \end{bmatrix} \begin{Bmatrix} w'' \\ \phi' \end{Bmatrix}. \tag{10}$$

If a coupling term is defined as $\Psi = K/\sqrt{EI \cdot GJ}$ as in Ref. [12], it has been shown that $-1 < \Psi < 1$. The magnitude of Ψ closing to ± 1 indicates the highly coupled situation while $\Psi = 0$ indicates no coupling between bending and torsion.

On the other hand, the classical laminated plate theory gives the relation between the plate bending moments, torsional moment and curvatures as

$$\begin{Bmatrix} M_x \\ M_y \\ M_{xy} \end{Bmatrix} = \begin{bmatrix} D_{11} & D_{12} & D_{16} \\ D_{12} & D_{22} & D_{26} \\ D_{16} & D_{26} & D_{66} \end{bmatrix} \begin{Bmatrix} \kappa_x \\ \kappa_y \\ \kappa_{xy} \end{Bmatrix}. \tag{11}$$

Following the paper by Weisshaar [12] the three stiffness parameters in Eq. (10) may be determined for high aspect ratio beams (assuming $M_x = 0$ but κ_x is not restrained) as

$$EI = b\left(D_{22} - \frac{D_{12}^2}{D_{11}}\right), \quad K = 2b\left(D_{26} - \frac{D_{12}D_{16}}{D_{11}}\right), \quad GJ = 4b\left(D_{66} - \frac{D_{16}^2}{D_{11}}\right), \tag{12}$$

where bending stiffnesses D_{11}, D_{22}, D_{66}, D_{12}, D_{16}, and D_{26} are given in Appendix A. It may be of interest to know that, for the assumption of chordwise rigidity ($w(x, y) = w(0, y) - x\phi(y), \kappa_x = 0$, but $M_x \neq 0$), the second term in Eq. (12) disappears and only the first term is left for EI, K, and GJ. This is equivalent to the situation that D_{11} tends to infinity, or infinite chordwise rigidity.

Once the stiffness parameters EI, K, and GJ are obtained, the free vibration of the coupled bending and torsion for the composite beam, with damping neglected, is governed by the

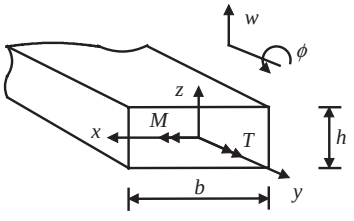

Fig. 3. A beam segment with the internal bending moment, torsional moment and deformations.

equations

$$EIw^{\mathrm{iv}} - K\phi''' + m\ddot{w} = 0, \quad GJ\phi'' - Kw''' - I_\alpha\ddot{\phi} = 0, \tag{13}$$

where m is the mass per unit length and I_α is the polar mass moment of inertia per unit length about y-axis.

Using separation of variables $w(y,t) = W(y)e^{i\omega t}$, $\phi(y,t) = \Phi(y)e^{i\omega t}$, Eq. (13) is transferred to the eigenproblem

$$EIW^{\mathrm{iv}} - K\Phi''' - m\omega^2 W = 0, \quad GJ\Phi'' - KW''' + I_\alpha\omega^2\Phi = 0. \tag{14}$$

As shown by Banerjee [15], eliminating either W or Φ in Eq. (14) will yield a general solution in the normalized form

$$\begin{aligned} W(\xi) &= A_1\cosh\alpha\xi + A_2\sinh\alpha\xi + A_3\cos\beta\xi + A_4\sin\beta\xi + A_5\cos\gamma\xi + A_6\sin\gamma\xi, \\ \Phi(\xi) &= B_1\cosh\alpha\xi + B_2\sinh\alpha\xi + B_3\cos\beta\xi + B_4\sin\beta\xi + B_5\cos\gamma\xi + B_6\sin\gamma\xi, \end{aligned} \tag{15}$$

where $A_{1\text{–}6}$ and $B_{1\text{–}6}$ are related by

$$\begin{gathered} B_1 = k_\alpha A_2/L, \quad B_2 = k_\alpha A_1/L, \quad B_3 = k_\beta A_4/L, \\ B_4 = -k_\beta A_3/L, \quad B_5 = k_\gamma A_6/L, \quad B_6 = -k_\gamma A_5/L \end{gathered}$$

and other parameters are defined consequently as

$$k_\alpha = (\bar{b} - \alpha^4)/(\bar{k}\alpha^3), \quad k_\beta = (\bar{b} - \beta^4)/(\bar{k}\beta^3), \quad k_\gamma = (\bar{b} - \gamma^4)/(\bar{k}\gamma^3),$$

with

$$\bar{k} = -K/EI,$$

$$\alpha = [2(q/3)^{1/2}\cos(\varphi/3) - a/3]^{1/2},$$

$$\beta = [2(q/3)^{1/2}\cos((\pi - \varphi)/3) + a/3]^{1/2},$$

$$\gamma = [2(q/3)^{1/2}\cos((\pi + \varphi)/3) + a/3]^{1/2},$$

$$q = b + a^2/3,$$

$$\varphi = \cos^{-1}[(27abc - 9ab - 2a^3)/2(a^2 + 3b)^{3/2}],$$

$$a = \bar{a}/c, \quad b = \bar{b}/c, \quad c = 1 - K^2/(EI \cdot GJ),$$

$$\bar{a} = I_\alpha\omega^2 L^2/GJ, \quad \bar{b} = m\omega^2 L^4/EI, \quad \xi = y/L.$$

Following Ref. [15], the expressions for the cross-sectional rotation $\Theta(\xi)$, the bending moment $M(\xi)$, the shear force $S(\xi)$ and the torsional moment $T(\xi)$ are obtained with the

normalized coordinate ξ as

$$\begin{aligned}\Theta(\xi) = (1/L)[&A_1\alpha \sinh \alpha\xi + A_2\alpha \cosh \alpha\xi - A_3\beta \sin \beta\xi \\ &+ A_4\beta \cos \beta\xi - A_5\gamma \sin \gamma\xi + A_6\gamma \cos \gamma\xi],\\ M(\xi) = (EI/L^2)[&A_1\bar{\alpha} \cosh \alpha\xi + A_2\bar{\alpha} \sinh \alpha\xi - A_3\bar{\beta} \cos \beta\xi \\ &- A_4\bar{\beta} \sin \beta\xi - A_5\bar{\gamma} \cos \gamma\xi - A_6\bar{\gamma} \sin \gamma\xi],\\ S(\xi) = -(EI/L^3)[&A_1\alpha\bar{\alpha} \sinh \alpha\xi + A_2\alpha\bar{\alpha} \cosh \alpha\xi + A_3\beta\bar{\beta} \sin \beta\xi \\ &- A_4\beta\bar{\beta} \cos \beta\xi + A_5\gamma\bar{\gamma} \sin \gamma\xi - A_6\gamma\bar{\gamma} \cos \gamma\xi],\\ T(\xi) = (GJ/L^2)[&A_1 g_\alpha \cosh \alpha\xi + A_2 g_\alpha \sinh \alpha\xi - A_3 g_\beta \cos \beta\xi \\ &- A_4 g_\beta \sin \beta\xi - A_5 g_\gamma \cos \gamma\xi - A_6 g_\gamma \sin \gamma\xi],\end{aligned} \tag{16}$$

where

$$\bar{\alpha} = \bar{b}/\alpha^2,\ \ \bar{\beta} = \bar{b}/\beta^2,\ \ \bar{\gamma} = \bar{b}/\gamma^2,$$

$$g_\alpha = (\bar{b} - c\alpha^4)/(\bar{k}\alpha^2),\ \ g_\beta = (\bar{b} - c\beta^4)/(\bar{k}\beta^2),\ \ g_\gamma = (\bar{b} - c\gamma^4)/(\bar{k}\gamma^2).$$

4. Eigenvalues and mode shapes of the cracked composite cantilever

Let the edge crack be located at $\xi_c = l/L$, as shown in Fig. 2. The cantilever beam is then replaced with two intact beams connected at the crack location by the local flexibility matrix. The solution of W and Φ for each intact beam can be expressed as follows:

Let $\Gamma = [\cosh \alpha\xi \ \ \sinh \alpha\xi \ \ \cos \beta\xi \ \ \sin \beta\xi \ \ \cos \gamma\xi \ \ \sin \gamma\xi]^{\mathrm{T}}$, then for $0 \leqslant \xi \leqslant \xi_c$,

$$W_1(\xi) = [A_1\ A_2\ A_3\ A_4\ A_5\ A_6]\Gamma,\ \ \Phi_1(\xi) = [B_1\ B_2\ B_3\ B_4\ B_5\ B_6]\Gamma, \tag{17a}$$

$\xi_c \leqslant \xi \leqslant 1$,

$$W_2(\xi) = [A_7\ A_8\ A_9\ A_{10}\ A_{11}\ A_{12}]\Gamma,\ \ \Phi_2(\xi) = [B_7\ B_8\ B_9\ B_{10}\ B_{11}\ B_{12}]\Gamma. \tag{17b}$$

There are 12 unknowns in Eq. (17) since B_{1-12} are related to A_{1-12} by the relationships (15). For the cantilever beam, the boundary conditions require that:

At the fixed end, $\xi = 0$,

$$W_1(0) = \Theta_1(0) = \Phi_1(0) = 0. \tag{18a–c}$$

At the free end, $\xi = 1$,

$$M_2(1) = S_2(1) = T_2(1) = 0. \tag{18d–f}$$

At the crack location, $\xi = \xi_c$, the local flexibility concept demands

$$\begin{aligned}&M_1(\xi_c) = M_2(\xi_c),\ \ S_1(\xi_c) = S_2(\xi_c),\ \ T_1(\xi_c) = T_2(\xi_c),\\ &W_2(\xi_c) = W_1(\xi_c) + c_{22}S_1(\xi_c) + c_{26}T_1(\xi_c),\\ &\Theta_2(\xi_c) = \Theta_1(\xi_c) + c_{44}M_1(\xi_c),\\ &\Phi_2(\xi_c) = \Phi_1(\xi_c) + c_{62}S_1(\xi_c) + c_{66}T_1(\xi_c).\end{aligned} \tag{18g–l}$$

Substitution of Eqs. (16) and (17) in Eq. (18) will yield the characteristic equation

$$[\Lambda]A = 0, \tag{19}$$

where $A = [A_1\ A_2\ A_3\ A_4\ A_5\ A_6\ A_7\ A_8\ A_9\ A_{10}\ A_{11}\ A_{12}]^{\mathrm{T}}$ and $[\Lambda]$ is the 12×12 characteristic matrix, a function of frequency.

Solving for $\det[\Lambda] = 0$ yields the natural frequencies. Substituting each natural frequency back to Eq. (19) will give the corresponding mode shape. Note that both the natural frequency and the mode shape now depend not only on the crack depth and location, but also on the material properties (fiber orientation and volume fraction).

One issue related to the coupled bending–torsion Eq. (13) is that, for the unidirectional composite beam in some specific fiber orientation (e.g. at 0° and 90°), bending and torsion will be decoupled such that Eq. (15) is no longer valid to solve for the eigenvalue problem. Under this situation the coupled equation simply reduces to two independent equations for bending and torsion after the separation of variables as

$$EIW^{\mathrm{iv}} - m\omega^2 W = 0, \quad GJ\Phi'' + I_\alpha \omega^2 \Phi = 0. \tag{20}$$

The general solution in the normalized form is

$$W(\xi) = A_1 \cosh \eta\xi + A_2 \sinh \eta\xi + A_3 \cos \eta\xi + A_4 \sin \eta\xi,$$
$$\Phi(\xi) = B_1 \cos \sigma\xi + B_2 \sin \sigma\xi,$$

where $\eta = (m\omega^2 L^4/EI)^{1/4}$, $\sigma = (I_\alpha \omega^2 L^2/GJ)^{1/2}$, and m and I_α are defined the same as in Eq. (13).

Similarly, let $\Gamma_1 = [\cosh \eta\xi\ \ \sinh \eta\xi\ \ \cos \eta\xi\ \ \sin \eta\xi]^{\mathrm{T}}$, $\Gamma_2 = [\cos \sigma\xi\ \ \sin \sigma\xi]^{\mathrm{T}}$, then for $0 \leqslant \xi \leqslant \xi_c$,

$$W_1(\xi) = [A_1\ A_2\ A_3\ A_4]\Gamma_1, \quad \Phi_1(\xi) = [B_1\ B_2]\Gamma_2, \tag{21a}$$

$\xi_c \leqslant \xi \leqslant 1$,

$$W_2(\xi) = [A_5\ A_6\ A_7\ A_8]\Gamma_1, \quad \Phi_2(\xi) = [B_3\ B_4]\Gamma_2. \tag{21b}$$

There are still 12 unknowns in Eq. (21). Again, the expressions for the cross-sectional rotation $\Theta(\xi)$, the bending moment $M(\xi)$, the shear force $S(\xi)$, and the torsional moment $T(\xi)$ become

$$\begin{aligned}
\Theta(\xi) &= (1/L)[A_1\eta \sinh \eta\xi + A_2\eta \cosh \eta\xi - A_3\eta \sin \eta\xi + A_4\eta \cos \eta\xi],\\
M(\xi) &= (EI/L^2)[A_1\eta^2 \cosh \eta\xi + A_2\eta^2 \sinh \eta\xi - A_3\eta^2 \cos \eta\xi - A_4\eta^2 \sin \beta\xi],\\
S(\xi) &= -(EI/L^3)[A_1\eta^3 \sinh \eta\xi + A_2\eta^3 \cosh \eta\xi + A_3\eta^3 \sin \eta\xi - A_4\eta^3 \cos \eta\xi],\\
T(\xi) &= (GJ/L^2)[-B_1\sigma \sin \sigma\xi + B_2\sigma \cos \sigma\xi].
\end{aligned} \tag{22}$$

The boundary conditions are the same as in Eq. (18). Substitution of Eqs. (21) and (22) in Eq. (18) yields the characteristic equation

$$[\Lambda]\bar{A} = 0, \tag{23}$$

where $\bar{A} = [A_1\ A_2\ A_3\ A_4\ A_5\ A_6\ A_7\ A_8\ B_1\ B_2\ B_3\ B_4]^{\mathrm{T}}$ and $[\Lambda]$ is still a 12×12 characteristic matrix.

The bending–torsion coupling described by Eq. (19) arises from both the equation of motion and the crack boundary condition. However, in Eq. (23) only the crack contributes to the coupling between bending and torsion that is initially decoupled by Eq. (20).

5. Results

The unidirectional composite beam consists of several plies aligned in the same direction. In each ply (and for the whole laminate) the material is assumed orthotropic with respect to its axes of symmetry. Material properties of each ply are taken to be: moduli of elasticity $E_m = 2.76\,\text{GPa}$, $E_f = 275.6\,\text{Gpa}$, Poisson's ratios $v_m = 0.33$, $v_f = 0.2$, moduli of rigidity $G_m = 1.036\,\text{GPa}$, $G_f = 114.8\,\text{Gpa}$, mass densities $\rho_m = 1600\,\text{kg/m}^3$, $\rho_f = 1900\,\text{kg/m}^3$. The subscript m stands for matrix and f for fiber. The geometry of the cantilever is taken to be: length $L = 0.5\,\text{m}$, width $b = 0.1\,\text{m}$, and height $h = 0.005\,\text{m}$. In the following sections, θ stands for the fiber angle, and V is the fiber volume fraction, $\eta = a/b$ the crack ratio, and $\xi_c = l/L$ the dimensionless crack location.

5.1. Coefficients of the local flexibility matrix

Once incorporated with the boundary conditions (18g–l), the components in the local flexibility matrix, Eq. (9), may be expressed in dimensionless formats for further comparison. The dimensionless constants become

$$\begin{aligned}
\bar{c}_{22} &= c_{22}\frac{EI}{L^3} = \varepsilon_{22}\Lambda_{\text{III}} \quad \text{with} \quad \varepsilon_{22} = \frac{2\pi D_3 EI}{hL^3},\\
\bar{c}_{44} &= c_{44}\frac{EI}{L} = \varepsilon_{44}\Lambda_1 \quad \text{with} \quad \varepsilon_{44} = \frac{24\pi D_1 Y_{\text{I}}^2 EI}{h^3 L},\\
\bar{c}_{66} &= c_{66}\frac{GJ}{L} = \varepsilon_{66}\Lambda_{\text{III}} \quad \text{with} \quad \varepsilon_{66} = \frac{576 D_3 \pi^7 h b^2 GJ}{(\pi^5 b h^2 - 192 h^3)^2 L},\\
\bar{c}_{26} &= c_{26}\frac{GJ}{L^2} = \varepsilon_{26}\Lambda_{\text{III}} \quad \text{with} \quad \varepsilon_{26} = \frac{96\pi^3 D_3 b GJ}{(\pi^5 b h^2 - 192 h^3) L^2},\\
\bar{c}_{62} &= c_{26}\frac{EI}{L^2} = \varepsilon_{62}\Lambda_{\text{III}} \quad \text{with} \quad \varepsilon_{62} = \frac{96\pi^3 D_3 b EI}{(\pi^5 b h^2 - 192 h^3) L^2},
\end{aligned} \tag{24}$$

where Λ_1 and Λ_{III} are dimensionless and defined the same as in Eq. (8). They are functions of crack ratio only ($a/b \in [0, 1]$) and both go to infinity with a/b approaching unity, as shown in Figs. 4 and 5. For a crack ratio close to 1, which means the beam is nearly completely broken, the beam dynamics suffer severe instability and these coefficients may not be able to describe its vibration characteristics. The following analysis is focused on the crack ratio up to 0.9.

Coefficients $\varepsilon_{22}, \varepsilon_{44}, \varepsilon_{66}, \varepsilon_{26}$, and ε_{62} are all dimensionless, and are functions of the fiber orientation, θ, and fiber volume fraction, V. Their variations are shown in Fig. 6.

It is obvious that coefficients $\varepsilon_{22}, \varepsilon_{44}, \varepsilon_{66}, \varepsilon_{26}$, and ε_{62} exhibit double symmetry for $\theta = 0^\circ$ and $V = 0.5$. Among these dimensionless coefficients, ε_{44} has the largest magnitude, followed by ε_{66} and then ε_{26} and ε_{62} with the last two accounting for the coupling effects. In other words, the bending or torsional mode is affected most by the internal bending or torsional moment, respectively, whose distribution along the beam has been altered by the surface crack. The internal shear force plays the least important role by noting its relatively low magnitude. The dimensionless Λ_1 and Λ_{III} work as "weighing" factors for the final

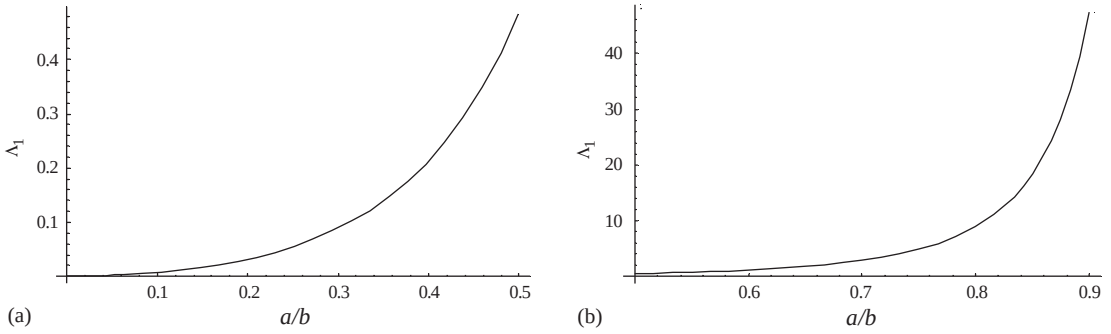

Fig. 4. The dimensionless coefficient Λ_1 as a function of the crack ratio a/b. (a) $a/b \in [0, 0.5]$, (b) $a/b \in [0.5, 1]$.

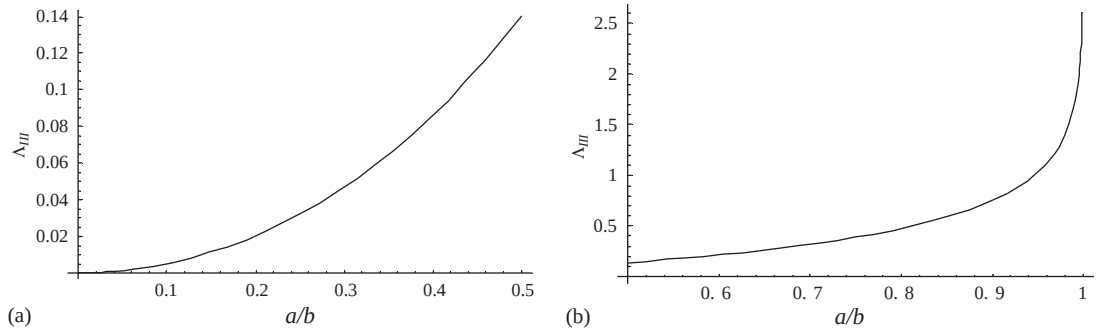

Fig. 5. The dimensionless coefficient Λ_{III} as a function of the crack ratio a/b. (a) $a/b \in [0, 0.5]$, (b) $a/b \in [0.5, 1]$.

dimensionless components in the local flexibility matrix. For a crack ratio up to 0.9, Λ_1 is always larger than Λ_{III} so that the role of the coefficient ε_{44} is further enhanced. Note that in Eq. (24) only $\bar{c}_{44}$ is affected by Λ_1.

As shown in Eq. (24) that coefficients $\varepsilon_{22}, \varepsilon_{44}, \varepsilon_{66}, \varepsilon_{26}$, and ε_{62} are normalized with either EI or GJ, a plot of each coefficient shown in Fig. 6 bears the similar "shape" as that of the normalized stiffness parameter EI or GJ as shown in Fig. 7.

5.2. The bending and torsional stiffness parameters, and the coupling term

The bending and torsional stiffness parameters, EI and GJ, are functions of θ and V, as shown in Fig. 7(a) and (c). For $\theta = 0^\circ$ or 90° (bending and torsion are decoupled), the torsional stiffness parameter GJ has the same variation with respect to the fiber volume fraction. However the bending stiffness parameter varies differently. When normalized by the stiffness at the fiber angle 0°, the dimensionless $EI(\theta, V)/EI(0, V)$ and $GJ(\theta, V)/GJ(0, V)$ are shown in Fig. 7(b) and (d).

The dimensionless coupling term Ψ, as defined by $\Psi = K/\sqrt{EI \cdot GJ}$, is the indication of how "strong" the bending and torsion are coupled, with ± 1 indicating the "strongest" coupling while

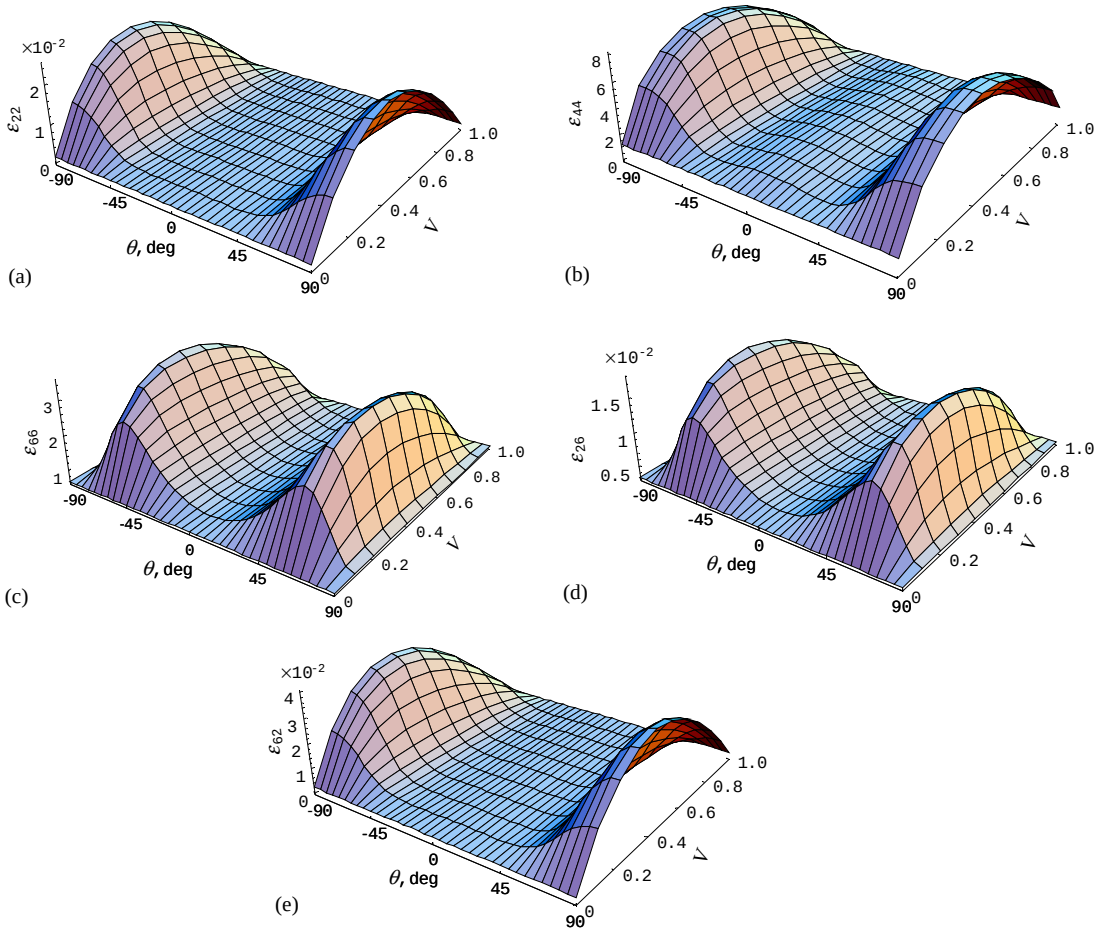

Fig. 6. Dimensionless coefficients in Eq. (24) as a function of the fiber angle (θ) and fiber volume fraction (V). (a) ε_{22}, (b) ε_{44}, (c) ε_{66}, (d) ε_{26}, (e) ε_{62}.

0 indicates no coupling. Fig. 7(e) shows the term with respect to the fiber angle and volume fraction. Bending and torsion are decoupled when $\theta = 0^\circ$ or 90°, or $V = 0$ or 1. For the fiber volume fraction being 0 or 1, the material is isotropic and homogeneous so that bending and torsion are basically decoupled for the beam with rectangular cross-section, and this is consistent with previously published results [9,10].

As shown in the figure, the "strong" coupling is expected for fiber angles around $\pm 65^\circ$, while the coupling is very "weak" for angles between $\pm 35^\circ$. The variation of the coupling term with respect to the fiber angle agrees with the results presented in Ref. [12]. Note that in Fig. 7 the stiffness parameters (EI and GJ) and the coupling term (Ψ) are determined by the fiber angle and fiber volume fraction, and no crack is involved.

Since the stiffness parameters as well as the coupling term are determined by the material properties (θ and V), natural frequencies of the cantilever will depend not only

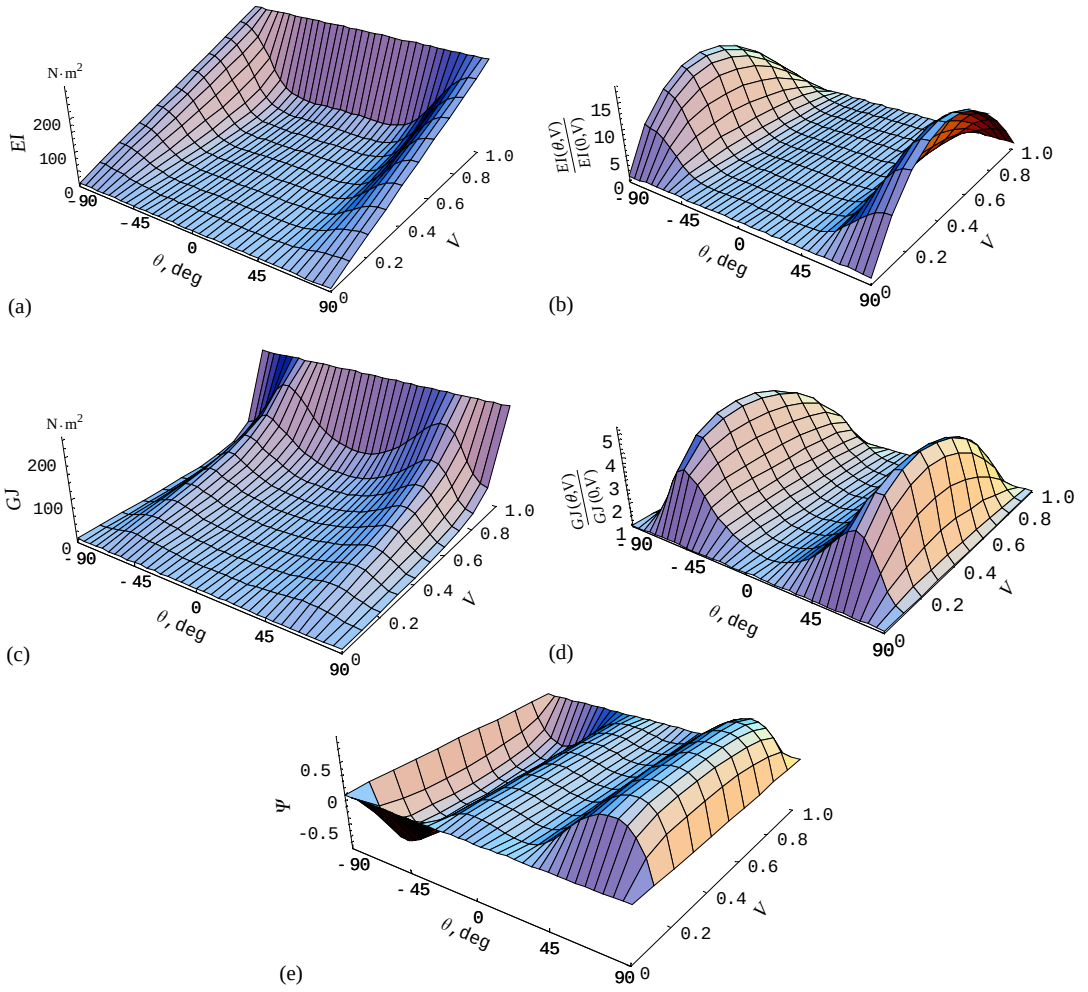

Fig. 7. The stiffness parameters and the coupling term as a function of the fiber angle (θ) and fiber volume fraction (V). (a) EI, (b) $EI/EI(0,V)$, (c) GJ, (d) $GJ/GJ(0,\ V)$, (e) Ψ. Note the regions of strong coupling corresponding to $\theta = \pm 65^{\circ}$.

on the crack location and its depth, but also on the material properties. The analysis of the natural frequency changes follows. Three situations are selected in terms of the degree of coupling.

5.3. Natural frequency change as a function of crack location, its depth and material properties (θ and V)

5.3.1. Natural frequency change as a function of crack ratio and fiber angle

Assume that the crack is located at $\xi_c = 0.3$ and the fiber volume fraction is $V = 0.5$. Natural frequencies will be affected by the crack ratio and fiber angle. The first four natural frequencies are plotted in Figs. 8–11.

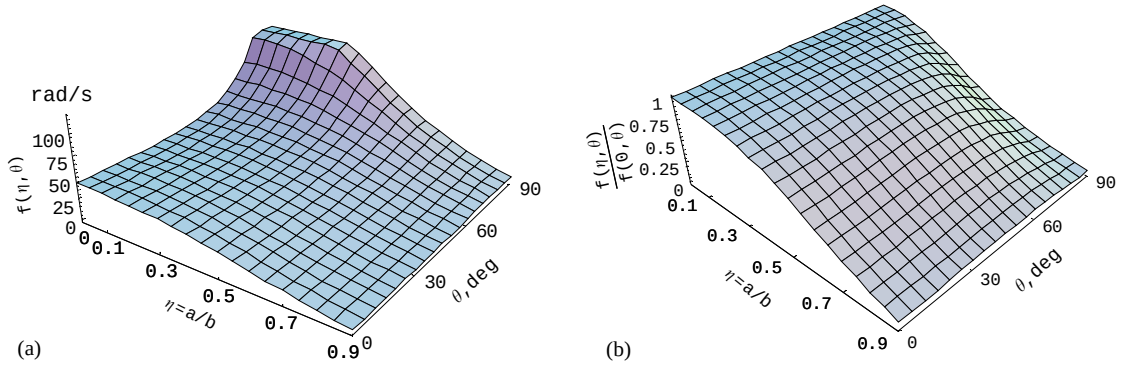

Fig. 8. Variation of the first natural frequency as a function of the crack ratio (a/b) and fiber angle (θ). (a) A direct plot, (b) normalized at $\eta = 0$ at the individual fiber angle.

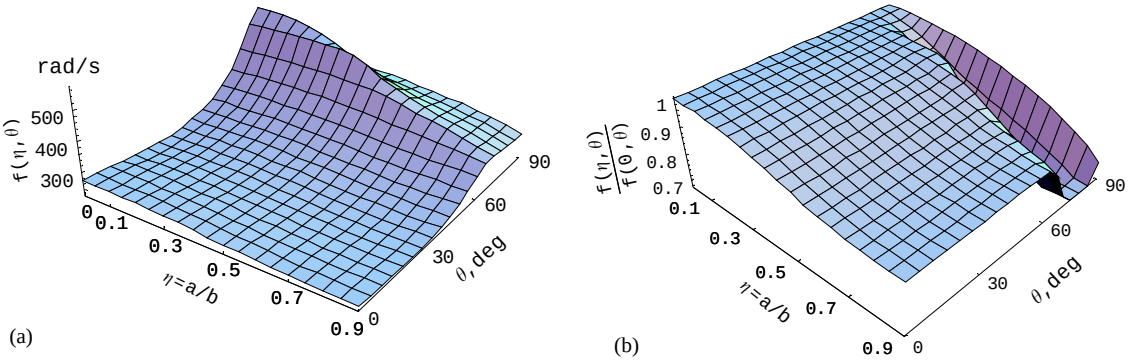

Fig. 9. Variation of the second natural frequency as a function of the crack ratio (a/b) and fiber angle (θ). (a) A direct plot, (b) normalized at $\eta = 0$ at the individual fiber angle.

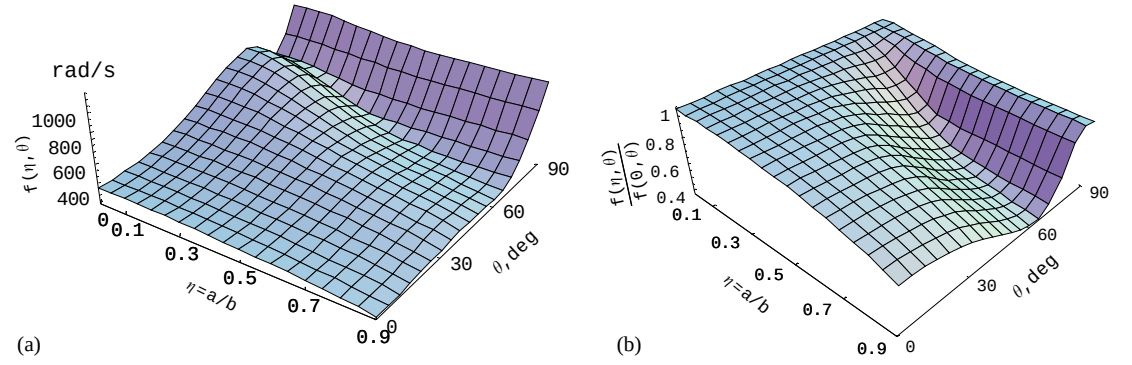

Fig. 10. Variation of the third natural frequency as a function of the crack ratio (a/b) and fiber angle (θ). (a) A direct plot, (b) normalized at $\eta = 0$ at the individual fiber angle.

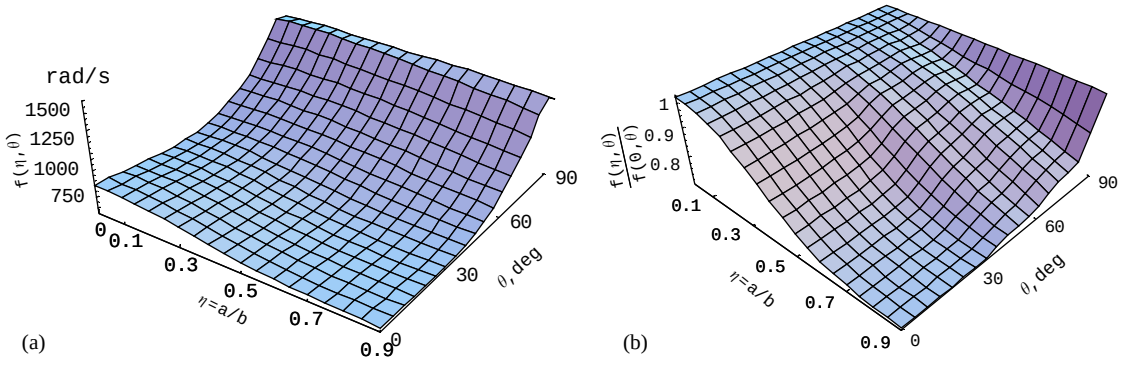

Fig. 11. Variation of the fourth natural frequency as a function of the crack ratio (a/b) and fiber angle (θ). (a) A direct plot, (b) normalized at $\eta = 0$ at the individual fiber angle.

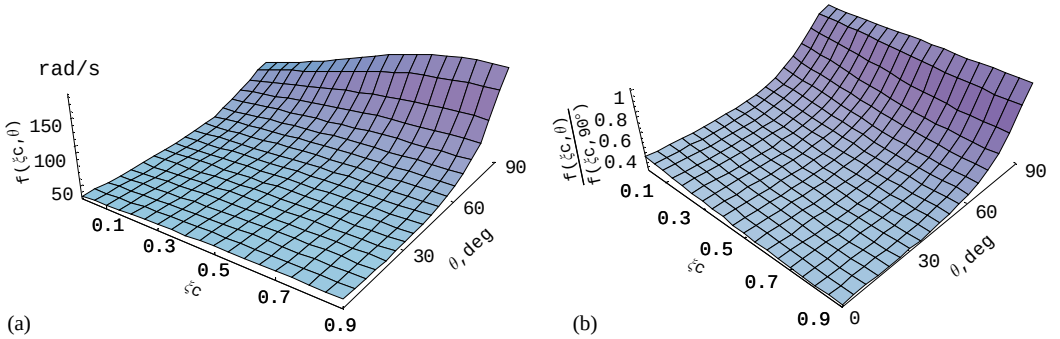

Fig. 12. Variation of the first natural frequency as a function of the normalized crack location (ξ_c) and fiber angle (θ). (a) A direct plot, (b) normalized at $\theta = 90^\circ$ at different crack location.

When the fiber angle is around 60°, where the bending and torsion are highly coupled, the frequency reduction with the crack ratio increased has a different pattern as that when the fiber angle is smaller. For instance, Figs. 9 and 10 indicate an accelerated reduction of the second and third frequencies with respect to the crack ratio in the region of $\theta = 60^\circ$. At a certain crack ratio, the natural frequency is controlled by either the bending or torsional mode when the fiber angle is small (the coupling is weak). However, when the fiber angle is increased such that the coupling becomes stronger, the same natural frequency which was previously controlled by the bending mode (or the torsional mode) becomes controlled by the torsional mode (or the bending mode). This could be the main reason for the transient region of the frequency reduction.

5.3.2. Natural frequency change as a function of crack location and fiber angle

Assume that the crack ratio is fixed at $\eta = 0.3$ and the fiber volume fraction is $V = 0.5$. Natural frequencies will be affected by the crack location and fiber angle. The first four natural frequencies are plotted in Figs. 12–15 as follows.

Similar to the results in Section 5.3.1 where the crack ratio and fiber angle are taken as variables, the frequency change when bending and torsion are highly coupled has a pattern

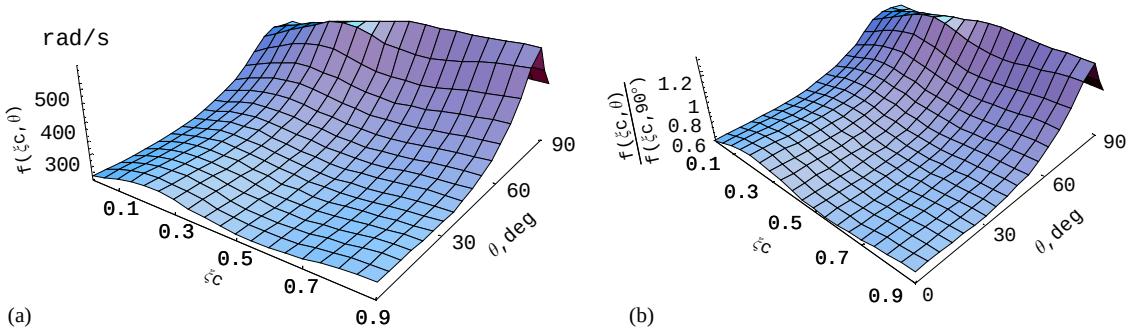

Fig. 13. Variation of the second natural frequency as a function of the normalized crack location (ξ_c) and fiber angle (θ). (a) A direct plot, (b) normalized at $\theta = 90^\circ$ at different crack location.

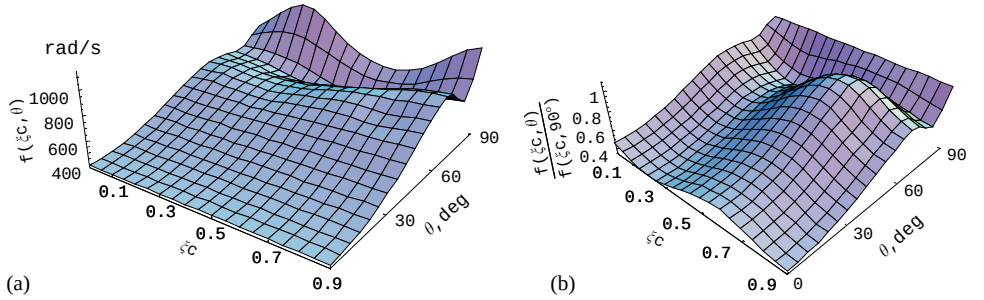

Fig. 14. Variation of the third natural frequency as a function of the normalized crack location (ξ_c) and fiber angle (θ). (a) A direct plot, (b) normalized at $\theta = 90^\circ$ at different crack location.

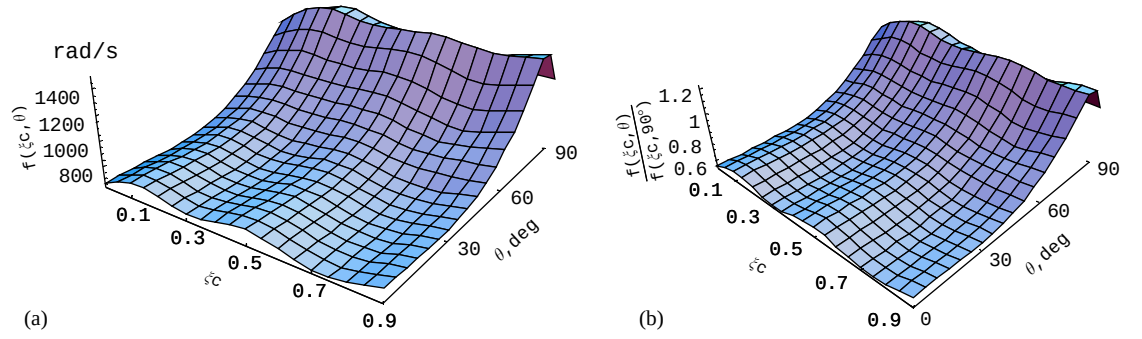

Fig. 15. Variation of the fourth natural frequency as a function of the normalized crack location (ξ_c) and fiber angle (θ). (a) A direct plot, (b) normalized at $\theta = 90^\circ$ at different crack location.

different from that when the coupling is "weak" at smaller fiber angles. When the fiber angle is fixed, the frequency change for different crack locations is affected by the corresponding mode shape.

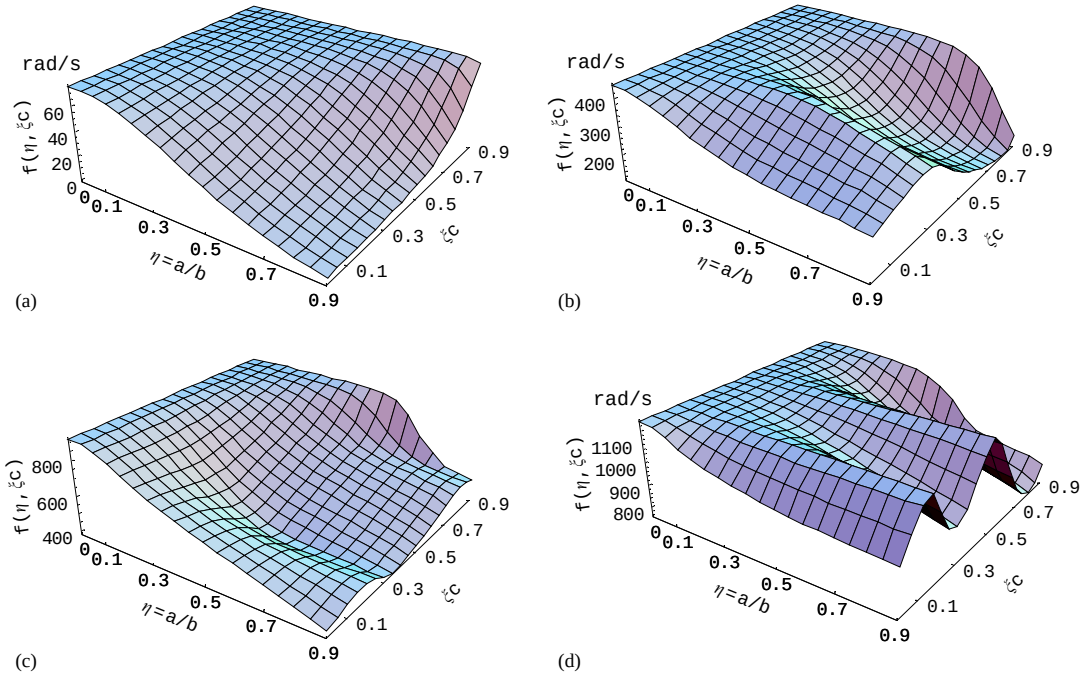

Fig. 16. Variation of natural frequencies as a function of the crack ratio (a/b) and normalized crack location (ξ_c) for the highly coupled situation due to material properties. (a) The first natural frequency ($f_{\text{intact}} = 75.2\,\text{rad/s}$), (b) the second natural frequency ($f_{\text{intact}} = 445.6\,\text{rad/s}$), (c) the third natural frequency ($f_{\text{intact}} = 916.1\,\text{rad/s}$), (d) the fourth natural frequency ($f_{\text{intact}} = 1179.7\,\text{rad/s}$).

5.3.3. *High coupling between bending and torsion*

Assume that $\theta = 70^\circ$ and $V = 0.5$. Bending and torsion are highly coupled with $\Psi = 0.846$. The natural frequency changes are plotted in Fig. 16.

In general the natural frequencies experience further reduction with the crack ratio increased. Fig. 16 indicates clearly that for a large crack ratio, the frequencies have different variation in terms of the crack location. As noticed in Refs. [9,10] where only bending vibration is investigated, the higher frequency reduction may be expected for the crack located around the largest curvature of the mode related to the frequency. While the trend is still shown in Fig. 16, the largest frequency reduction no longer coincides with either the largest bending curvature or torsion curvature, since the bending and torsional modes usually do not have the largest curvature or node at the same location.

5.3.4. *Low coupling between bending and torsion, and bending–torsion decoupled*

When $\theta = 30^\circ$ and $V = 0.5$, bending and torsion are weakly coupled with $\Psi = 0.0545$. The natural frequency changes are plotted in Fig. 17.

It is obvious that the third natural frequency does not show the similar variation as that in Fig. 16(c) of Section 5.3.3 where bending and torsion are highly coupled. When the coupling due to the material properties is weak (i.e. the coupling term Ψ is very small), the frequency variation

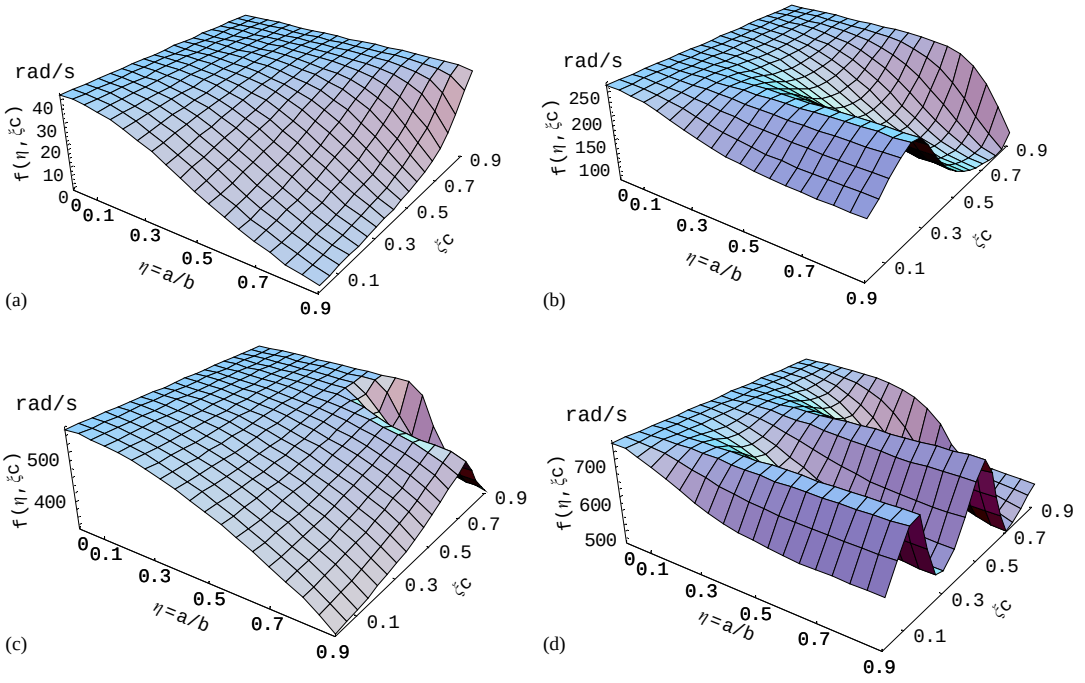

Fig. 17. Variation of natural frequencies as a function of the crack ratio (a/b) and normalized crack location (ξ_c) for the weakly coupled situation due to material properties. (a) The first natural frequency ($f_{\text{intact}} = 42.35\,\text{rad/s}$), (b) the second natural frequency ($f_{\text{intact}} = 265.42\,\text{rad/s}$), (c) the third natural frequency ($f_{\text{intact}} = 554.38\,\text{rad/s}$), (d) the fourth natural frequency ($f_{\text{intact}} = 743.41\,\text{rad/s}$).

exhibits quite the similar feature as that where bending and torsion are initially decoupled due to the material properties, and then coupled only due to the presence of the crack. The frequency variation for the latter case is shown in Fig. 18.

When $\theta = 0^\circ$ or 90°, the bending and torsion are decoupled if there are no cracks. The natural frequencies for bending and torsion are listed in Table 1.

However, presence of an edge crack introduces coupling through the additional boundary condition at the crack location. For $\theta = 0^\circ$ and $V = 0.5$, the natural frequency changes are plotted in Fig. 18 as a function of the crack ratio and its location.

When the coupling of bending and torsion is introduced by the crack only (no coupling if there was no crack), the third natural frequency has very similar variation as that of the first natural frequency. The coupled natural frequency is predominantly controlled by either the bending mode or the torsional mode, while the surface crack introduces only a "weak" coupling between bending and torsion. The third coupled frequency is actually close to the first torsional frequency so that the variation is quite close to that of the first coupled frequency that is controlled by the first bending mode.

For the situation shown in Fig. 17 where coupling due to material properties is "weak", the coupling seems predominantly controlled by the local flexibility due to the crack such that the frequency variation exhibits a similar trend as in Fig. 18.

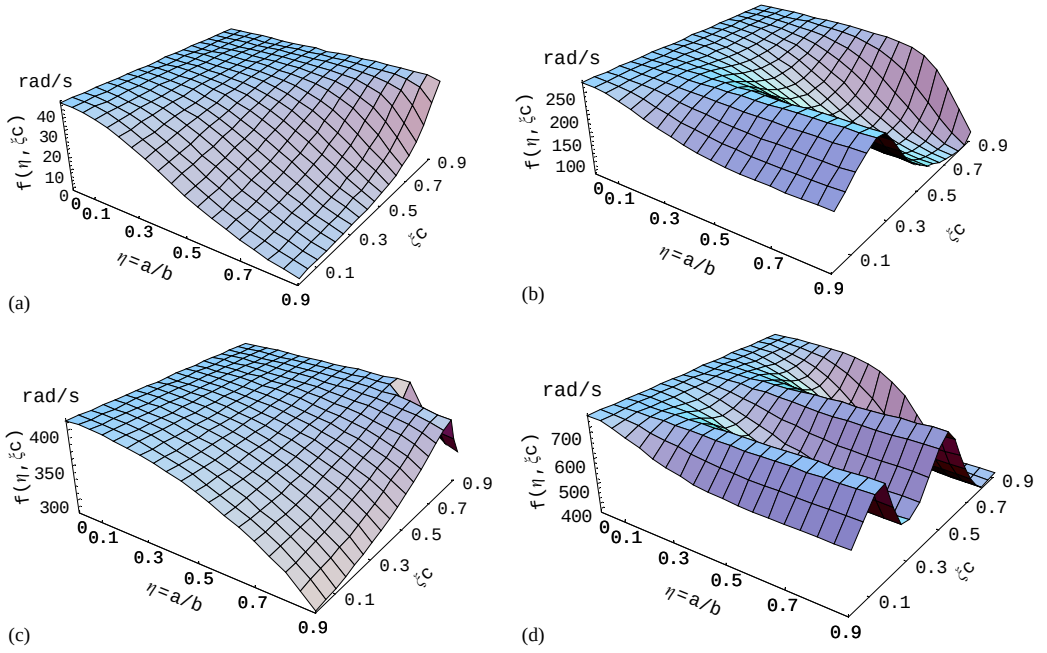

Fig. 18. Variation of natural frequencies as a function of the crack ratio (a/b) and the normalized crack location (ξ_c) for situation that the coupling is introduced by the crack only. (a) The first natural frequency, (b) the second natural frequency, (c) the third natural frequency, (d) the fourth natural frequency.

Table 1
The first five natural frequencies for $\theta = 0^\circ$ and 90°

rad/s	$\theta = 0^\circ$					$\theta = 90^\circ$				
	1st	2nd	3rd	4th	5th	1st	2nd	3rd	4th	5th
Bending	43.6	273.1	764.7	1498.5	2477.2	181.0	1134.5	3176.7	6225.0	10290.4
Torsion	413.5	1240.6	2067.7	2894.7	3721.8	413.5	1240.6	2067.7	2894.7	3721.8

5.4. Mode shape changes

For theoretical analysis, the change of mode shapes may help detect the crack location as well as its magnitude, in conjunction with the change of natural frequencies. In the situation of highly coupled bending and torsion ($\theta = 70^\circ$ and $V = 0.5$ as in Section 5.3.3) due to the material properties, the first three mode shapes are plotted in Figs. 19–24 for different crack depths and locations.

5.4.1. For crack at location $\xi_c = 0.2$

In Figs. 19–24, each mode shape is obtained with the crack ratio at 0.2, 0.4, and 0.6, while the crack ratio of 0 indicates no cracks.

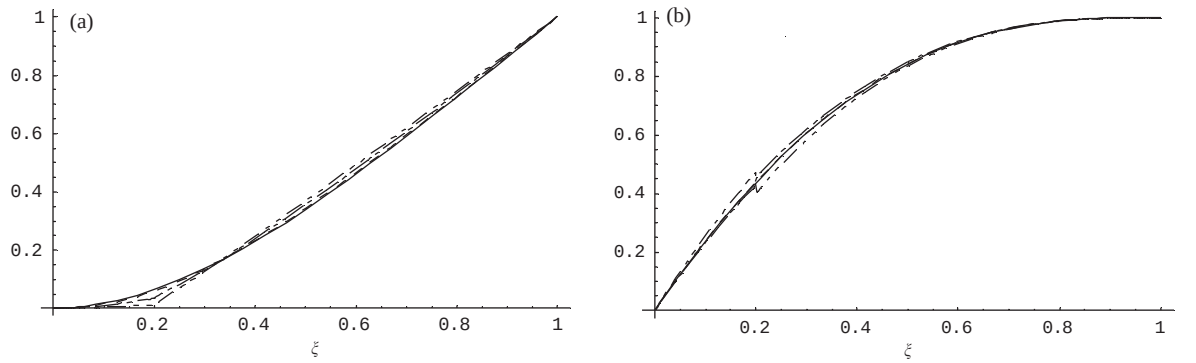

Fig. 19. The first mode shapes for $\xi_c = 0.2$, $V = 0.5$, and $\theta = 70^\circ$ as the crack ratio (η) changes. ——, $\eta = 0$; – – – – –, $\eta = 0.2$; - · - · - · -, $\eta = 0.4$; – · · – · ·, $\eta = 0.6$. (a) The first bending mode, (b) the first torsional mode. Note that the discontinuity increases with the crack ratio at the crack location.

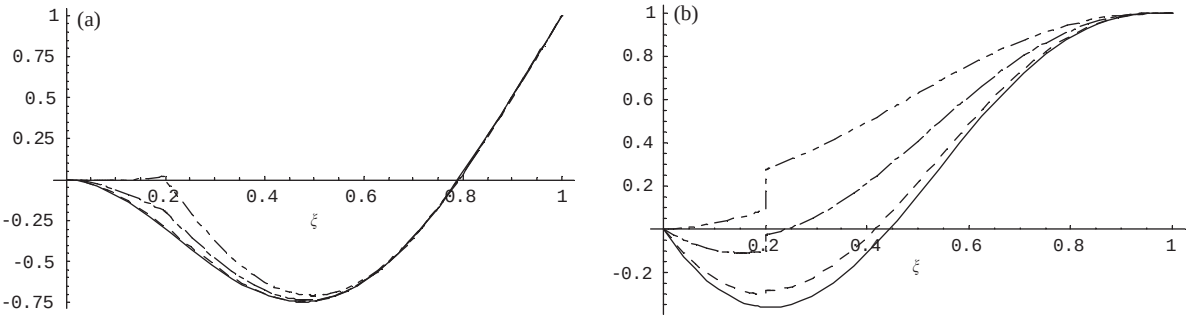

Fig. 20. The second mode shapes for $\xi_c = 0.2$, $V = 0.5$, and $\theta = 70^\circ$ as the crack ratio (η) changes. ——, $\eta = 0$; – – – – –, $\eta = 0.2$; - · - · - · - · -, $\eta = 0.4$; – · · – · ·, $\eta = 0.6$. (a) The second bending mode, (b) the second torsional mode.

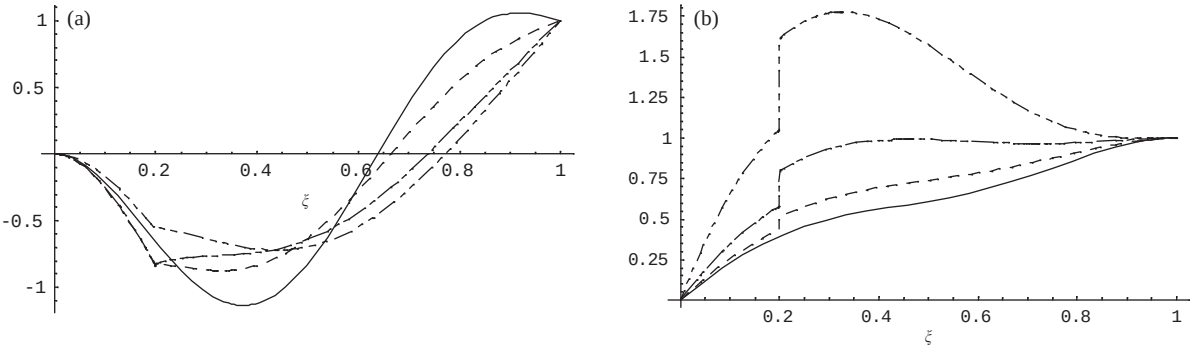

Fig. 21. The third mode shapes for $\xi_c = 0.2$, $V = 0.5$, and $\theta = 70^\circ$ as the crack ratio (η) changes. ——, $\eta = 0$; – – – – –, $\eta = 0.2$; - · - · - · - · -, $\eta = 0.4$; – · · – · ·, $\eta = 0.6$. (a) The third bending mode, (b) the third torsional mode.

Each of the first three modes is normalized by the value at the free end of the cantilever. The higher mode seems more sensitive to the crack depth, even though the crack is not located at the large curvature position. The discontinuity of the torsional mode is more obvious than the

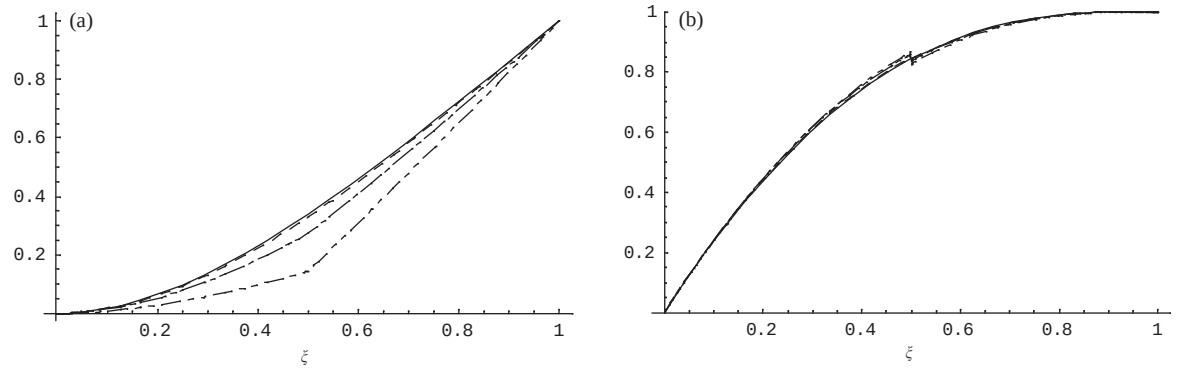

Fig. 22. The first mode shapes for $\xi_c = 0.5$, $V = 0.5$, and $\theta = 70^\circ$ as crack ratio (η) changes. ——, $\eta = 0$;– – – – –, $\eta = 0.2$; - · - · - · - · - , $\eta = 0.4$; – · · – · · , $\eta = 0.6$. (a) The first bending mode, (b) the first torsional mode. Note that the discontinuity increases with the crack ratio at the crack location.

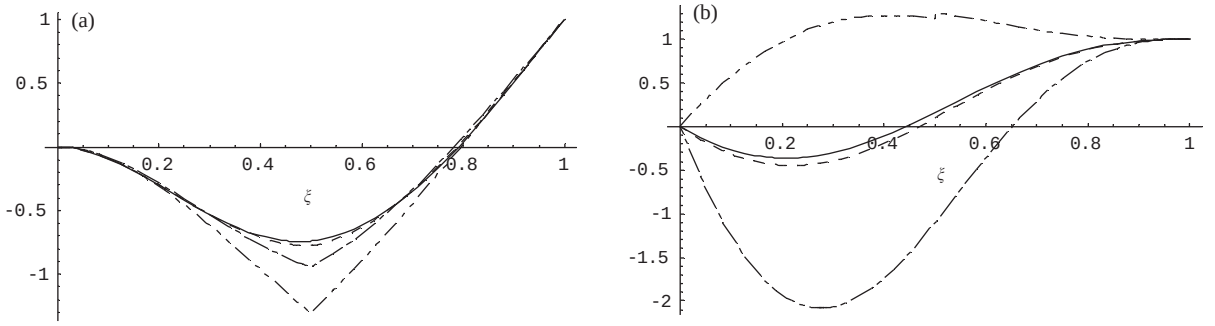

Fig. 23. The second mode shapes for $\xi_c = 0.5$, $V = 0.5$, and $\theta = 70^\circ$ as the crack ratio (η) changes. ——, $\eta = 0$; – – – – –, $\eta = 0.2$; - · - · - · - · - , $\eta = 0.4$; – · · – · · , $\eta = 0.6$. (a) The second bending mode, (b) the second torsional mode.

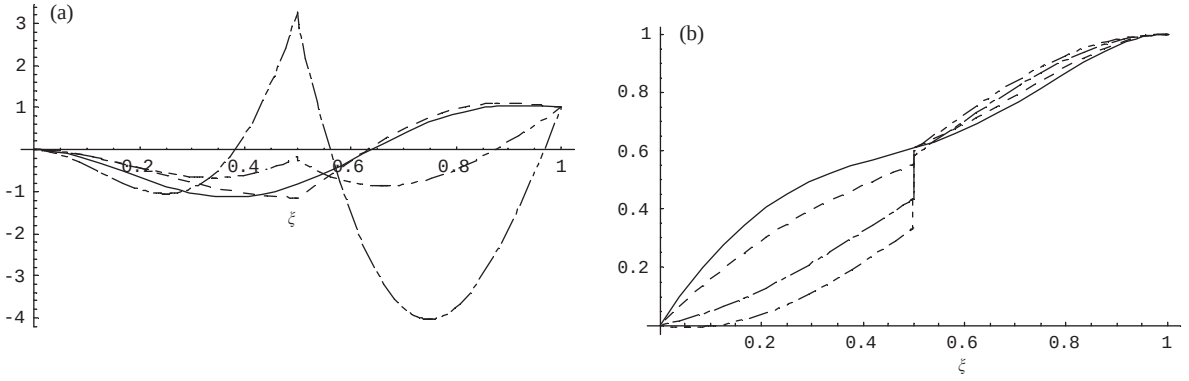

Fig. 24. The third mode shapes for $\xi_c = 0.5$, $V = 0.5$, and $\theta = 70^\circ$ as the crack ratio (η) changes. ——, $\eta = 0$; – – – – –, $\eta = 0.2$; - · - · - · - · - , $\eta = 0.4$; – · · – · · , $\eta = 0.6$. (a) The third bending mode, (b) the third torsional mode.

bending mode. Since the characteristic equation consists of 12 simultaneous equations, any small deviation from the exact frequency solution changes the magnitude of the mode shape a lot (especially for the torsional modes). However, the shape and increasing distortion at the crack location may still be of value to detect the crack location, particularly when both bending and torsional modes are taken into consideration.

5.4.2. For crack at location $\xi_c = 0.5$

For the crack located at the mid-point of the cantilever, distortion of higher mode shapes is even more obvious. Compared with those where only the bending mode, either for the Euler–Bernoulli beam or for the Timoshenko beam, is studied, the change of mode shapes due to the crack for the composite beam with bending and torsion coupled is more significant. This change may be utilized to locate the crack as well as to quantify its magnitude.

6. Conclusion

A composite cantilever beam with an edge crack and of high aspect ratio vibrates in coupled bending and torsional modes, either due to the material properties, due to the crack or both. The beam consists of several fiber-reinforced plies with all fibers orientated in the same direction. The local flexibility approach based on linear fracture mechanics is taken to model the crack and a local compliance matrix at the crack location is derived. Changes in natural frequencies and mode shapes are investigated. Some observations include:

(1) The dimensionless coefficients of the compliance matrix exhibit double symmetry with respect to the fiber orientation and fiber volume fraction. The internal bending moment distribution due to the crack affects the bending mode most significantly through the local flexibility matrix; the effect is the same for the torsional mode; the internal shear force distribution plays the least role in the local flexibility.
(2) The decrease of natural frequencies for a cracked composite beam depends not only on the crack location and its depth, but also on the material properties, as shown in Ref. [9] for an Euler–Bernoulli beam. However, for the composite cantilever with bending and torsional modes coupled, the largest frequency reduction no longer coincides with either the largest bending or torsion curvatures.
(3) The "strong" coupling between the bending and torsion is observed for fiber angles around $\pm 60^\circ$, while the coupling is "weak" for fiber angles between $\pm 35^\circ$. The frequency variation with respect to either the crack ratio or its location usually experiences a transient state when the coupling is "strong", such that the pattern is significantly different from the "weakly" coupled case. At this transient state the frequency variation previously controlled mainly by the bending mode (or the torsional mode) becomes controlled by the torsional mode (or the bending mode).
(4) When the fiber angle is 0 or $\pm 90^\circ$, bending and torsion are decoupled if there is no crack. The edge crack introduces the coupling to the initially uncoupled bending and torsion. The decrease of natural frequencies exhibits a similar pattern as that when the fiber angle is

between $\pm 35^{\circ}$; the pattern is predominantly controlled by either bending or torsional mode, but not both.

(5) The coupled mode shapes are more sensitive to both the crack location and its depth. Higher modes exhibit more distortion at the crack location.

An analytical model of a fiber-reinforced composite beam with an edge crack has been developed. The spectrum of the natural frequency reduction, along with observations on the mode shape changes indicated by this model, may be used to detect both the crack location and its depth for on-line structural health monitoring. When the cracked beam vibrates with a specific loading spectrum, the model presented in this paper may help analyze the stress distribution around the crack tip such that a crack propagation model may be developed to investigate damage prognosis, and make predictions regarding the behavior of the structure to future loads. For instance these results may be useful for predicting flutter speed reduction in aircraft with composite wings due to fatigue cracking.

Acknowledgements

The first two authors gratefully acknowledge financial support for this research by Los Alamos National Laboratory under the grant 44238-001-0245.

Appendix A. Material properties of a single ply

The complex constants μ_1, μ_2 in Eq. (2) are roots of the characteristic equation [1]

$$\bar{A}_{11}\mu^4 - 2\bar{A}_{16}\mu^3 + (2\bar{A}_{12} + \bar{A}_{66})\mu^2 - 2\bar{A}_{26}\mu + \bar{A}_{22} = 0, \tag{A.1}$$

where the compliances $\bar{A}_{11}$, $\bar{A}_{22}$, $\bar{A}_{12}$, $\bar{A}_{16}$, $\bar{A}_{26}$, $\bar{A}_{66}$ are defined by

$$\bar{A}_{11} = A_{11}m^4 + (2A_{12} + A_{66})m^2n^2 + A_{22}n^4,$$

$$\bar{A}_{22} = A_{11}n^4 + (2A_{12} + A_{66})m^2n^2 + A_{22}m^4,$$

$$\bar{A}_{12} = (A_{11} + A_{22} - A_{66})m^2n^2 + A_{12}(m^4 + n^4),$$

$$\bar{A}_{16} = (2A_{11} - 2A_{12} - A_{66})m^3n - (2A_{22} - 2A_{12} - A_{66})mn^3,$$

$$\bar{A}_{26} = (2A_{11} - 2A_{12} - A_{66})mn^3 - (2A_{22} - 2A_{12} - A_{66})m^3n,$$

$$\bar{A}_{66} = 2(2A_{11} + 2A_{22} - 4A_{12} - A_{66})m^2n^2 + A_{66}(m^4 + n^4),$$

with $m = \cos\theta, n = \sin\theta$, and θ being the angle between the geometric axes of the beam (x–y) and the material principle axes (1–2) as shown in Fig. 2. The roots are either complex or purely imaginary, and cannot be real. The constants μ_1 and μ_2 correspond to those with positive imaginary parts.

Constants A_{11}, A_{22}, A_{12}, A_{66} are compliance elements of the composite along the principle axes and directly relate to the mechanical constants of the material [16]. Under the plane strain condition,

$$A_{11} = \frac{1}{E_{11}}\left(1 - \frac{E_{22}}{E_{11}}v_{12}^2\right), \quad A_{22} = \frac{1}{E_{22}}(1 - v_{23}^2), \quad A_{12} = -\frac{v_{12}}{E_{11}}(1 + v_{23}).$$

Under the plane stress condition,

$$A_{11} = \frac{1}{E_{11}}, \ A_{22} = \frac{1}{E_{22}}, \ A_{12} = -\frac{v_{12}}{E_{11}} = -\frac{v_{21}}{E_{22}}.$$

To study the third crack mode, other compliances for both the plane strain and plane stress can be found to be

$$A_{44} = \frac{1}{G_{23}}, \quad A_{55} = A_{66} = \frac{1}{G_{12}}.$$

The mechanical properties of the composite, E_{11}, E_{22}, v_{12}, v_{23}, G_{12}, G_{23}, ρ, can be found [1] to be

$$E_{11} = E_f V + E_m(1 - V), \ E_{22} = E_{33} = E_m\frac{E_f + E_m + (E_f - E_m)V}{E_f + E_m - (E_f - E_m)V},$$

$$v_{12} = v_{13} = v_f V + v_m(1 - V),$$

$$v_{23} = v_{32} = v_f V + v_m(1 - V)\frac{1 + v_m - v_{12}E_m/E_{11}}{1 - v_m^2 + v_m v_{12}E_m/E_{11}},$$

$$G_{12} = G_{13} = G_m\frac{G_f + G_m + (G_f - G_m)V}{G_f + G_m - (G_f - G_m)V},$$

$$G_{23} = \frac{E_{22}}{2(1 + v_{23})}, \ \rho = \rho_f V + \rho_m(1 - V),$$

where subscript m stands for matrix and f for fiber. V is the fiber volume fraction.

Also based on the mechanical properties determined above as well as the ply orientation, the bending stiffness D_{ij} in Eq. (11) can be determined [17] by

$$D_{11} = Q_{11}m^4 + Q_{22}n^4 + 2(Q_{12} + 2Q_{66})m^2n^2,$$

$$D_{22} = Q_{11}n^4 + Q_{22}m^4 + 2(Q_{12} + 2Q_{66})m^2n^2,$$

$$D_{12} = (Q_{11} + Q_{22} - 4Q_{66})m^2n^2 + Q_{12}(m^4 + n^4),$$

$$D_{16} = mn[Q_{11}m^2 - Q_{22}n^2 - (Q_{12} + 2Q_{66})(m^2 - n^2)],$$

$$D_{26} = mn[Q_{11}n^2 - Q_{22}m^2 + (Q_{12} + 2Q_{66})(m^2 - n^2)],$$

$$D_{66} = (Q_{11} + Q_{22} - 2Q_{12})m^2n^2 + Q_{66}(m^2 - n^2)^2,$$

where

$$Q_{11} = \frac{E_{11}}{1 - v_{12}v_{21}} I, \quad Q_{22} = \frac{E_{22}}{1 - v_{12}v_{21}} I, \quad Q_{12} = Q_{11}v_{21}I = Q_{22}v_{12}I, \quad Q_{66} = G_{12}I,$$

with $I = h^3/12$ the unit width cross-sectional area moment of inertia of the beam.

Appendix B. The stress along the short edge of a rectangular cross-section

Consider the beam with rectangular cross-section as shown in Fig. 2 for stress analysis under the torsional moment T. With $b > h$, the stress distribution on the cross-section can be found in the classical theory of elasticity. Specifically the stress along the short edge, $\tau_{yz}|_{x=\pm b/2}$, can be found [18] to be

$$\tau_{yz}\big|_{x=\pm b/2} = \frac{8h}{\pi^2}\mu\alpha \sum_{n=0}^{\infty}\left[\frac{(-1)^n}{(2n+1)^2}\frac{\sinh(k_n \pm b/2)}{\cosh(k_n b/2)}\cos(k_n z)\right], \tag{B.1}$$

where $k_n = (2n+1)\pi/h$, and $\mu\alpha$ relates to the torsional moment by

$$T = \mu\alpha\left(\frac{bh^3}{3} - \frac{64h^4}{\pi^5}\sum_{n=0}^{\infty}\frac{\tanh(k_n b/2)}{(2n+1)^5}\right). \tag{B.2}$$

For $b/h > 2$, $1 > \tanh(\pi b/2h) > 0.9963$, truncating the series in Eqs. (B.1) and (B.2) with the first term will result in 92% and 99.5% accuracy of the analytical solution for the stress and moment, respectively. With only the first term in both summations along with the approximation $\tanh(\pi b/2h) = 1$, eliminating $\mu\alpha$ in Eqs. (B.1) and (B.2) and taking the magnitude of the stress along the short edge yield

$$\tau_{yz} = \frac{24T\pi^3}{\pi^5 bh^2 - 192h^3}\cos\left(\frac{\pi}{h}z\right).$$

References

[1] G.C. Sih, E.P. Chen, *Mechanics of Fracture, Vol. 6: Cracks in Composite Materials*, Martinus Nijhoff, Dordrecht, 1981.
[2] J. Wauer, Dynamics of cracked rotors: a literature survey, *Applied Mechanics Review* 17 (1991) 1–7.
[3] A.D. Dimarogonas, Vibration of cracked structures: a state of the art review, *Engineering Fracture Mechanics* 55 (5) (1996) 831–857.
[4] P. Cawley, R.D. Adams, A vibration technique for non-destructive testing of fiber composite structures, *Journal of Composite Materials* 13 (1979) 161–175.
[5] A.D. Dimarogonas, S.A. Paipetis, *Analytical Method of Rotor Dynamics*, Elsevier Applied Science Publishers, London, 1983.
[6] K. Nikpour, A.D. Dimarogonas, Local compliance of composite cracked bodies, *Composites Science and Technology* 32 (1988) 209–223.
[7] K. Nikpour, Buckling of cracked composite columns, *International Journal of Solids and Structures* 26 (12) (1990) 1371–1386.
[8] K. Nikpour, Diagnosis of axisymmetric cracks in orthotropic cylindrical shells by vibration measurement, *Composites Science and Technology* 39 (1990) 45–61.

[9] M. Krawczuk, W.M. Ostachowicz, Modeling and vibration analysis of a cantilever composite beam with a transverse open crack, *Journal of Sound and Vibration* 183 (1) (1995) 69–89.
[10] O. Song, T. Ha, L. Librescu, Dynamics of anisotropic composite cantilevers weakened by multiple transverse open cracks, *Engineering Fracture Mechanics* 70 (2003) 105–123.
[11] J.B. Kosmatka, J. Panza, Aeroelastic stability of the GA-ASI Predator aircraft, *AIAA's First Technical Conference and Workshop on Unmanned Aerospace Vehicles AIAA-2002-3470*, Portsmouth, VA, May 2002.
[12] T.A. Weisshaar, Vibration tailoring of advanced composite lifting surfaces, *Journal of Aircraft* 22 (2) (1985) 141–147.
[13] G. Bao, S. Ho, Z. Sou, B. Fan, The role of material orthotropy in fracture specimens for composites, *International Journal of Solids and Structures* 29 (1992) 1105–1116.
[14] H. Tada, P.C. Paris, G.R. Irwin, *The Stress Analysis of Cracks Handbook*, 3rd ed., ASME Press, New York, 2000.
[15] J.R. Banerjee, Explicit analytical expressions for frequency equation and mode shapes of composite beam, *International Journal of Solids and Structures* 38 (2001) 2415–2426.
[16] R.M. Jones, *Mechanics of Composite Materials*, Scripta Book Company, Washington, DC, 1975.
[17] J.R. Vinson, R.L. Sierakowski, *Behavior of Structures of Composed of Composite Materials*, Martinus Nijhoff, Dordrecht, 1991.
[18] I.S. Sokolnikoff, *Mathematical Theory of Elasticity*, Krieger, New york, 1983.